Synthesis of tunable gold nanostars via 3D printed microfluidic device with vibrating sharp tip acoustic mixing

Kathrine Curtin[1], Toktam Godary[2], Peng Li[2*]

[1] Department of Mechanical and Aerospace Engineering, West Virginia University, Morgantown, WV, USA
[2] C. Eugene Bennett Department of Chemistry, West Virginia University, Morgantown, WV, USA.
* Correspondence and requests for materials should be addressed to P.L. **(peng.li@mail.wvu.edu)**

Abstract

Gold nanostars are valuable materials for nanomedicine, energy conversation, and catalysis. Microfluidic synthesis offers a simple and controlled means to produce nanoparticles as they offer precise fluid control and improve heat and mass transfer. 3D printed microfluidics are a good alternative to PDMS devices because they are affordable to produce and can be more easily integrated with active mixing strategies. 3D printed microfluidics have only been applied to the production of silver and gold nanospheres, but not complex structures like gold nanostars. Synthesis of gold nanostars requires highly effective mixing to ensure uniform nucleation and growth. In this work, we present a 3D-printed microfluidic device that utilizes an efficient vibrating sharp tip acoustic mixing system to produce high-quality and reproducible gold nanostars via a seedless and surfactant-free method. The vibrating sharp-tip mixing device can mix three streams of fluid across ~300 μm within 7 ms. The device operates with flow rates ranging from 10 μL min to 750 μL/min at low power requirements (2 – 45 mW). The optical properties of the resulting nanotars are easily tuned from 650 nm to 800 nm by modulating the input flow rate. Thus, the presented 3D printed microfluidic device produces high-quality gold nanostars with tunable optical and physical properties suitable for extensive applications.

Keywords: microfluidic, 3D printing, nanoparticle synthesis, gold nanostar, acoustofluidics

Competing Interests: The authors declare no competing financial or non-financial interests.

Introduction

With the growth in nanomedicine, continuous-flow microfluidic devices have emerged as a platform for nanomaterials production and synthesis. Large scale or bulk synthesis techniques suffer from batch-to-batch variability, so synthesizing nanoparticles in microfluidic devices offers widespread advantages due to the difficulty in controlling the reaction stoichiometry. Microfluidics are compact, simple to operate, and eliminate costly instruments and laborious operations. (Tofighi et al. 2017; Kimura et al. 2018; Herbst et al. 2019) They can be easily automated and offer a high degree of fluid control. By scaling down reactions to the microscale, heat and mass transfer are improved, which enables the production of precise nanostructures with fine control of sizes, shapes, and morphology. (Ma et al. 2017) Microfluidic devices have been applied for the synthesis of lipid,(Jahn et al. 2010; Belliveau et al. 2012; Maeki et al. 2015) metallic, (Boleininger et al. 2006; Sebastian Cabeza et al. 2012; Uson et al. 2016) and polymeric nanoparticles.(Valencia et al. 2010; Li et al. 2016)

Conventionally used PDMS microfluidic devices suffer from several disadvantages for nanoparticle production. PDMS device fabrication requires extensive manual operations, which limits scalability and hinders its commercial translation. (Bandulasena et al. 2017; Bressan et al. 2020) 3D printed microfluidic devices are a good alternative platform because they can be rapidly and affordably produced without multistep protocols. 3D printed devices using passive Y-mixer and T-junctions were applied for the synthesis of silver and gold nanospheres (Kitson et al. 2012; Bressan et al. 2019; Andrea Cristaldi et al. 2021). For these continuous flow devices, throughput was low, as the maximum flow rate was ~200 µL/min. To date, complex metallic nanostructures, such as gold nanostars, have not been synthesized using 3D printed microfluidics. Complex structures, like gold nanostars are an important type of metallic nanoparticles because of their strong tunable optical absorption for optical, biomedical, and catalytic applications. (Pandey et al. 2013; Chen et al. 2015) Gold nanostars are conventionally synthesized using either seeded (Kumar et al. 2007; Khoury and Vo-Dinh 2008; D. Ramsey et al. 2015) or seedless (Minati et al. 2014; Silvestri et al. 2017; Liebig et al. 2019) bulk synthesis techniques. Seedless methods are much simpler and offer single-step reactions, but effective mixing is critical for uniform nucleation. Droplet microfluidics-based methods have been used for gold nanostar synthesis to produce high quality nanostars.(Abalde-Cela et al. 2018; Illath et al. 2023) While droplet microfluidic strategies reduce reaction volume to improve mixing and kinetics, samples must be post-processed to remove oil, which is not a trivial task.

In this work, we present a 3D printed microfluidic device integrated with an acoustically driven vibrating sharp tip capillary for gold nanostar synthesis. The advantages of this device are threefold for gold nanostar synthesis: 1) the device enables high efficiency mixing at a wide range of flow rates; 2) allows for precise reagent concentration control in a single step for optical property tuning; 3) and is easy to fabricate using 3D printing. The acoustic mixing demonstrates rapid mixing as fast as 7 ms over short mixing lengths (300 µm) and does not require manual operation.(Li et al. 2021) The mixing performance facilitates rapid mass transport across the microfluidic channel to produce gold nanostars.(Huang et al. 2019) The present device offers simple acoustic mixing integration for application with 3D printed devices. The three-inlet design allows for simple

control of $AgNO_3$, ascorbic acid, and gold precursor flow rates, where users can produce gold nanostars with varied optical properties in a single, programmable step. The 3D printed microfluidic device produced high-quality nanostars with tunable optical properties. The nanostars were synthesized to achieve localized surface plasmon resonance (LSPR) absorptions ranging from 650 nm to 800 nm with 14-27 branches. Lastly, 3D printing is a much more accessible technology and makes device fabrication simple and affordable.

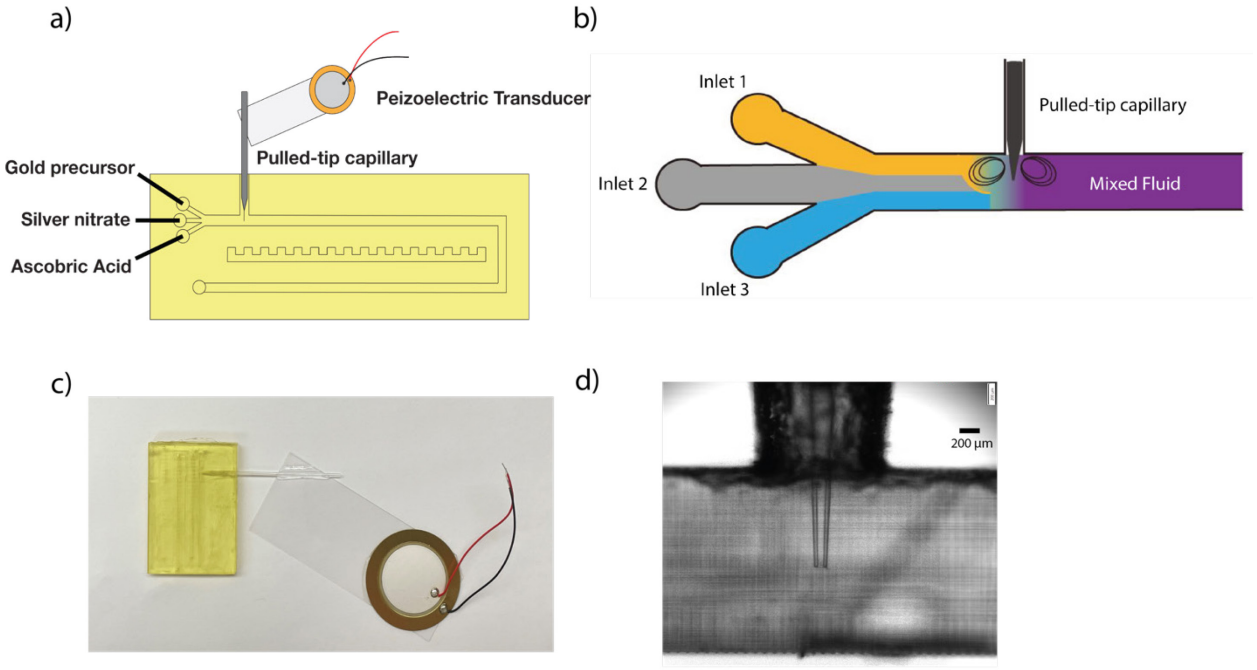

Figure 1 Vibrating sharp-tip capillary device overview a) device schematic b) microfluidic mixing working principle c) device image d) pulled-tip capillary in the microfluidic channel

Experimental Section

Materials and Reagents

Poly (ethylene glycol) diacrylate (PEGDA, MW 250), phenylbis (2,4,6-trimethylbenzoyl) phosphine oxide (Irgacure 819), fluorescein, ascorbic acid, silver nitrate, and gold (III) chloride trihydrate were purchased from Sigma−Aldrich (St. Louis, MO, USA). 2-nitrophenyl phenyl sulfide (NPS) was purchased from TCI (Tokyo, Japan). Isopropanol (IPA) was purchased from Fisher Scientific (Pittsburgh, PA, USA). Ultra-Ever Dry super-hydrophobic coating was purchased from Ultratech. Water was purified using a Merck Millipore purification system (Bedford, MA, USA). Norland Optical Adhesive were purchased from Norland Products (Jamesburg, New Jersey, USA). Epoxy glue (5-minute epoxy, Devcon) was purchased from ITW (Glenview, IL, USA).

Microfluidic Device Fabrication

The sharp tip mixer microfluidic device was fabricated using digital light processing (DLP) 3D printing for high resolution, low cost, and rapid printing. An Asiga Pico2 HD 3D printer with LED peak wavelength of 385 nm, an X-Y plane resolution of 37 µm and a Z-axis

control of 1 μm was used. 3D structures of the microfluidic device were designed using SolidWorks and uploaded to the 3D printer. The device channel dimensions were: 500 μm width, 500 μm height, and 2.78 cm length. The side channel for capillary insertion is 1.2 mm in diameter. Devices were printed using PEGDA 250 with 0.5% (w/w) Irgacure 819 and 0.5% (w/w) nitrophenyl phenyl sulfide (NPS). The build layer thickness was set to 50 μm, 0.8 s. After the 3D printing was completed, the device was immediately washed with isopropanol and water. It was then cured with UV light at 365 nm for 5 minutes. After curing, the device was secured to a glass slide using epoxy glue. After the glue is applied, the glass slide is held in place on the 3D printed device using binder clips. The pressure applied by the binder clips ensures the glass side does not move and keeps the glass slide uniformly flat along the 3D printed surface during drying. To prevent liquid leakage from the pulled-tip glass capillary side channel, the inner surface of the side channel was carefully coated using a two-step superhydrophobic coating (Figure S1). The superhydrophobic coating reagent, Ultra Ever Dry Bottom Coat was carefully applied using a 10 μL pipette. The bottom layer was allowed to dry for 1 hour prior to application of the Ultra Ever Dry Top Coat. The topcoat was applied using a pipette and was allowed to dry for 2 hours.

The sharp tip mixing device was prepared by securing a piezoelectric transducer (7BB-27-4L0, Murata, Kyoto, Japan) to a glass cover slip using epoxy glue. The pulled-tip glass capillary was prepared by pulling precision capillary tubes (OD: 0.87 mm, Drummond Scientific, Broomall, PA, USA) using a laser-based micropipette puller (PUL-1000, World Precision Instruments, FL, USA). The pulled-tip capillary was secured to the corner of the glass cover slip using glass glue at a 30° angle as shown in Fig. 1 in accordance with our previous works (Ranganathan et al. 2019, He et al. 2021, Li et al. 2021). After the acoustic transducer and sharp tip device were prepared, the capillary outer surface was coated using the two-step superhydrophobic coating and carefully inserted into the side channel (Figure S1). Microscope observation monitored this step to prevent the sharp tip from breaking against channel walls. Once inserted, the device was ready for further use.

Mixing Characterization

The establish the optimum mixing efficiency, we followed the protocol outlined in our previous work.[24] Briefly, two inlets of the sharp tip mixing device were infused with a stream of fluorescein solution and water at 30 μL/min. The third inlet was plugged using tubing attached to a syringe, as it was not needed for this experiment. The piezoelectric transducer was turned on to begin sharp tip vibration. The piezoelectric transducer was driven by Tektronix function generator (AFG1062) connected to an amplifier (LZY-22+, Mini-Circuits). To determine the mixing frequency, the excitation frequency was varied from 70 kHz to 100 kHz in 100 Hz increments. Under Olympus IX-73 inverted fluorescence microscope observation, the fluorescent signal was tracked and imaged downstream from the sharp tip. The downstream position was selected as the cross section immediately downstream of the sharp tip. Fluorescent cross-section was measured using ImageJ for each position, and the mixing index was calculated by dividing the standard deviation of the intensity by the mean intensity. An index of < 0.1 indicated effective mixing, with the frequency providing the best mixing index. Each sharp tip capillary exhibits an optimum mixing frequency which typically ranges between 90 kHz

and 100 kHz. The determined optimal frequency was then used to assess the operational amplitudes across various flow rates. The device was infused with different total flow rates, and mixing was conducted at amplitudes varying between 1 V_{pp} and 15 V_{pp}. The lowest amplitude resulting in the lowest mixing index was selected as the operating amplitude. At the lowest effective amplitude condition for each flow rate, the mixing length was measured. The mixing length was defined as the region from the last point of no mixing to the first point of full mixing along the channel.

Instrumentation

UV-Visible spectra were collected using a Shimadzu UV-1800 UV/Visible Scanning Spectrophotometer from 400 nm to 950 nm. The nanostars were imaged with transmission electron microscopy (JEOL JEM-2100F) at 200 kV. Sharp tip mixing was observed using an Olympus IX-73 inverted fluorescence microscope. Two syringe pumps (Fusion 200, Chemyx Inc., Stafford, TX) were used for reagent injection.

Bulk nanostar synthesis

Gold nanostars were synthesized using a modified bulk chemical synthesis. In brief, aqueous 2 mM gold precursor, 4 mM AgNO3, and 1.6 mM ascorbic acid solutions were freshly prepared. To synthesize particles of different number of branches and core size, the ratio of gold:silver:reducing agent were varied by volume. The desired volumes of silver and gold were gently mixed and followed by rapid injection of the reducing agent with a pipette. The solution quickly changed color upon the addition of ascorbic acid, indicating the formation of nanoparticles. The reaction was allowed to proceed for 20 minutes, then the solution was centrifuged at 2000 rpm for 8 minutes and washed twice with DI water. After washing, the nanostars were stored at 4°C.

Vibrating sharp-tip microfluidic device nanostar synthesis

Gold nanostars were synthesized using the reagents prepared for the bulk synthesis previously described. To synthesize the nanostars using the microfluidic sharp tip mixer, each reagent was loaded into a 1 mL syringe. The syringes were loaded onto syringe pumps (Fusion 200, Chemyx Inc., Stafford, TX) and desired flow rates were set. The tubing was secured to each fluid inlet on the microfluidic device. The signal generator and amplifier were set to the optimum mixing settings and turned on. The pumps were then turned on to start fluid flow through the microfluidic device. The ratios of gold:silver:reducing agent were changed by modifying the respective flow rate. As synthesis was conducted the resulting nanostars were collected in a microtube using tubing from the device outlet. After 10 minutes of synthesis, the sharp-tip mixer and syringe pumps were turned off and the gold nanostar solution collected in a centrifuge tube was removed from the device. The nanostars were centrifuged at 2000 rpm for 8 minutes and washed twice with DI water. The products were stored at 4°C until further use. The device can be reused after each synthesis, and each device was used at least 4 times in this study.

Results and Discussion

Device design and rationale

In this work, we used a modified surface and seed-free synthesis method that uses silver nitrate, ascorbic acid, and gold precursor. (Silvestri et al. 2017; Marelli et al. 2020) While surfactants provide nanoparticle stability, surfactants like PVP and CTAB can be challenging to remove from the particle surface. Surfactants can yield particles toxic in biological applications and can make it difficult to modify surfaces. (Nehl et al. 2006) For seedless nanostar synthesis, Yuan et al. indicates that silver ions and ascorbic acid must be added to the reaction at the same time to prevent silver precipitation and large nanosphere nucleation. (Yuan et al. 2012) While using microfluidics allows precise control of reagent flow and synthesizing nano stars in continuous flow manner, it requires fast mixing to ensure a uniform reaction. Here, we designed a microfluidic device with a three-inlet system to infuse silver nitrate, ascorbic acid, and $HAuCl_4$, respectively. As the solutions are infused, they pass through the acoustically driven sharp tip mixing, where the streams are rapidly mixed, and gold nanostar growth is initiated. The concentration of reagents and their ratios are easily controlled by modulating the input flow rates, which facilitates fine optical tuning of the resulting nanostars.

Mixing Performance

Device mixing performance is integral for nanoparticle synthesis. Our first step was to evaluate the device mixing performance and determine the device operating conditions. We characterized the mixing performance in terms of mixing length, mixing time, velocity, and mixing index across flow rate and operating conditions. Mixing behavior and performance were evaluated by infusing the device with streams of fluorescein and DI water, which enabled mixing visualization through fluorescence microscopy. **Fig. 2a** shows fluorescence microscopy images of the acoustic device when the device is turned “off” and “on.” and indicates the mixing length for mixing time calculation.

The total flow rate of the device determines the nanoparticle synthesis throughput, so it is important for the device to operate across a range of flow rate conditions. When the total flow rate is changed, the voltage must be adjusted to maintain effective mixing. So, the working flow rates of the mixer are influenced by the input voltage on the device. We used mixing index to quantitatively measure the mixing performance at different flow rate and voltage conditions. Flow rates within the device were tested from 30 μL/min to 750 μL/min. The mixing index was calculated for each flow rate and voltage ranging from 1 Vpp to 15 Vpp. The mixing index was calculated as the standard deviation of the fluorescent intensity divided by the mean intensity. The operating voltage was selected as the minimum voltage required to produce a mixing index of 0.1 or less. As shown in **Fig. 2b,** for a single flow rate the mixing index is decreased as the voltage is increased because the increase in driving voltage induces more effective mixing. For each flow rate, there is a minimum voltage where the mixing index is 0.1 or less. This minimum voltage is impacted by the total flow rate. For example, when the flow rate is increased from 30 μL/min to 120 μL/min, the minimum required voltage is increased from 3 Vpp to 5 Vpp (**Fig. 2b**). By simply increasing the voltage, we can operate the device across flow rates from 30 μL/min to 750 μL/min (**Fig. 2c**). As flow rate increases, the voltage must be adjusted to component for the change in total flow rate.

For nanoparticle synthesis, rapid mixing time across a short mixing length is essential for achieving uniform nanoparticle nucleation, which ultimately impacts size distribution. For our device, the mixing length is the distance from the last unmixed position to the first fully mixed position. The mixing length across flow rates ranged from 550 µm to 300 µm. As flow rate was increased, there is a slight decrease in the mixing length (**Table S1**). From the mixing length, we calculated the mixing time by:

$$T = LWH/R$$

Where L is the mixing length (Figure 2a), W is the channel width, H is the channel height, and R is the volumetric flow rate. The mixing time across flow rates is shown in **Fig. 2d**. As the flow rate increases in the device, the mixing time is sharply decreased. For example, when the flow rate is at 10 µL/min the mixing time is 881 ms and when the flow rate is increased to just 60 µL/min the mixing time is significantly reduced to 161 ms. The lowest mixing time achieved in this study was 7 ms.

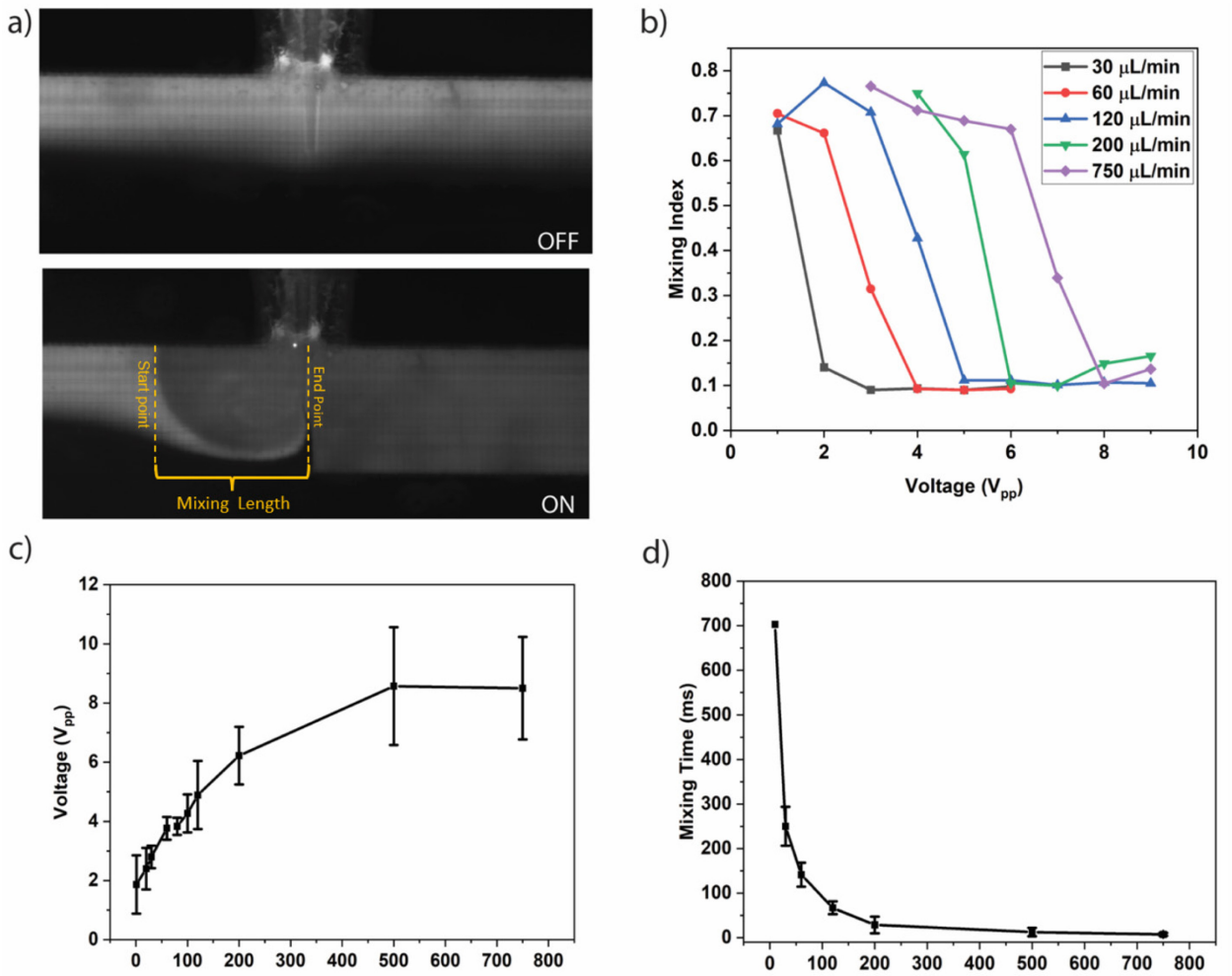

Figure 2. Characterization of mixing performance of vibrating sharp tip mixing device across flow rates. a) image of fluorescein and water infusion with vibrating sharp tip mixer "OFF" and "ON" b) Relationship between mixing index and the input voltage at five flow

rate conditions c) Influence of total flow rate on the minimum voltage required for effective mixing d) Influence of total flow rate on the mixing time. Error bars represent the standard deviation of 3 independent trials.

Gold nanostar synthesis in vibrating sharp tip capillary microfluidic device

Upon evaluation of the mixing performance of the vibrating sharp-tip microfluidic device, we synthesized gold nanostars using the device. In this work, we used a modified surfactant and seed-free synthesis that uses silver nitrate, ascorbic acid, and gold precursor, where the ascorbic acid reduces gold to trigger nanostar growth. (Silvestri et al. 2017; Marelli et al. 2020)

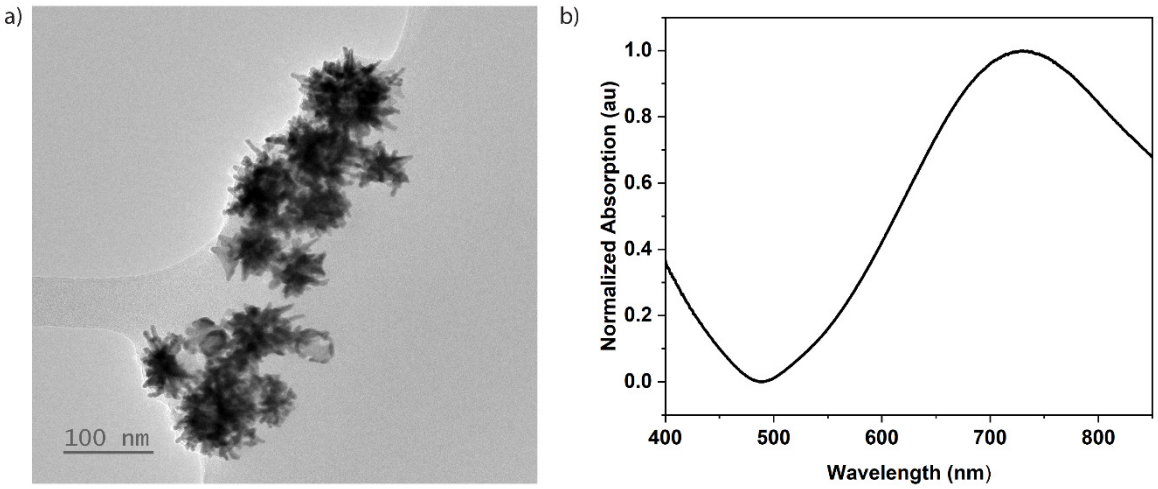

Figure 3. Characterization of gold nanostars synthesized with vibrating sharp tip device using ratio gold precursor: silver nitrate: ascorbic acid flow rate ratios of 30:30:70 µL/min. a) TEM micrograph b) UV-Visible spectrum

Gold nanostars were synthesized in the microfluidic device using a single constant flow rate condition to demonstrate synthesis. The flow rates for gold precursor and silver nitrate were each set at 30 µL/min, while the flow rate for ascorbic acid was set to 70 µL/min. This condition gives an effective molar ratio of 3:3:7 for gold: silver nitrate: ascorbic acid. After collecting the solution from the outlet for 5 minutes, the nanostars were washed using ultracentrifugation, the UV-Visible spectrum was measured for the nanostars, and they were imaged using TEM to observe the morphology (**Figure 3 and Figure S2**). Under these conditions, the resulting gold nanostars were hyperbranched with an average of 14 ± 2 branches and 78 nm in diameter when measured from branch to branch. These nanostars exhibited an optical absorption peak at 735 nm. The optical absorption from the nanostars synthesized in our device offers optical absorption between 700 nm and 800 nm, which is comparable to other reported in the literature (Nehl et al. 2006).

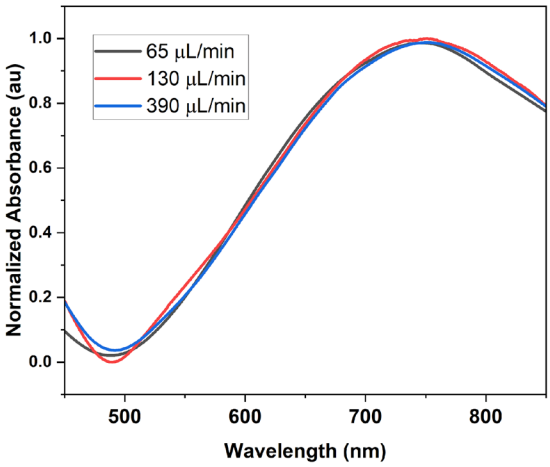

Figure 4. UV-Visible spectra of gold nanostars synthesized with vibrating sharp tip device for total flow rates of 65 µL/min, 130 µL/min, and 390 µL/min.

After demonstrating successful nanostar synthesis, we investigated the impact of the total flow rate on the resulting nanostars since the total flow rate impacts the residence time on the device and subsequent growth time (**Fig. 4**). In our synthesis, nucleation occurs immediately upon complete mixing because of the uniform distribution of the ascorbic acid to reduce the gold precursor. As noted by other works, nucleation in our synthesis was indicated by the immediate color change to blue (Chatterjee et al. 2016; Phiri et al. 2019). Nanostars were synthesized using three total flow rates (65 µL/min, 130 µL/min and 390 µL/min) to demonstrate residence and growth times of 15 minutes, 7.5 minutes, and 2.5 minutes. 1 mL of sample for each flow rate was synthesized and immediately washed using ultracentrifugation and resuspension. The resulting UV-Visible spectra show good agreement for the three samples with optical absorption at 740 nm. From this result, we see that flow rates ranging from 65 to 390 µL/min does not have a significant impact on the nanostar growth. Regardless of the total flow rate, the mixing device achieves a mixing time sufficient to trigger uniform nucleation, as seen by the consistency in the UV-Visible spectra. In addition, nanostar growth is also a rapid process that is not impacted by the incubation time in the device. Both nanostar nucleation and growth occur quickly and uniformly in the device because the mixing device is efficiently distributing the three precursors throughout the channel. Uniform distribution ensures reagent availability and prevents non-uniform nucleation that would cause spectral variations. The properties of resulting nanostars are independent of total flow rates in this flow rate range. Therefore, the present method is very flexible in adjusting flow rates to suit different needs of synthesis throughput. It should be noted that the post processing method is critical for nanostar morphology. When using a surfactant-free technique, there is concern for particle reshaping over extended periods of time. When our nanostars were not washed after two hours, the nanostars exhibited blue-shift in the UV-Visible spectra, indicating destabilization of the nanostar shape (**Fig. S3**). In this case, nanostars undergo Ostwald ripening to reduce the high surface energy associated with the anisotropic branches (Vang and Strobbia 2023). However, when the nanostars are washed to remove excess precursors, the products are highly stable (**Fig. S3**). The UV-Visible spectrum for the

washed nanostars is consistent with the spectrum from the “as-synthesized” sample. This result indicates that after two hours the washed nanostar sample is not undergoing Ostwald ripening and is highly stable. The experiment shows that washing must be done upon synthesizing the nanostars to prevent reshaping and destabilization.

Effect of ascorbic acid and silver nitrate on nanostar synthesis

The present method offers a continent means of adjusting the molar ratio of different reagents, which may allow synthesizing different properties of nanostars in one experiment run. The three-inlet design enables users to control flow rates for each precursor in the synthesis. By modulating the flow rate ratios of each precursor, the ratio and concentration can be controlled for each experimental condition. It has been reported that the concentration of silver ions and ascorbic acid in the reaction influences the resulting nanostar size and morphology. Here, we investigated the properties of nanostars synthesized with different concentrations of silver ions and ascorbic acid, respectively.

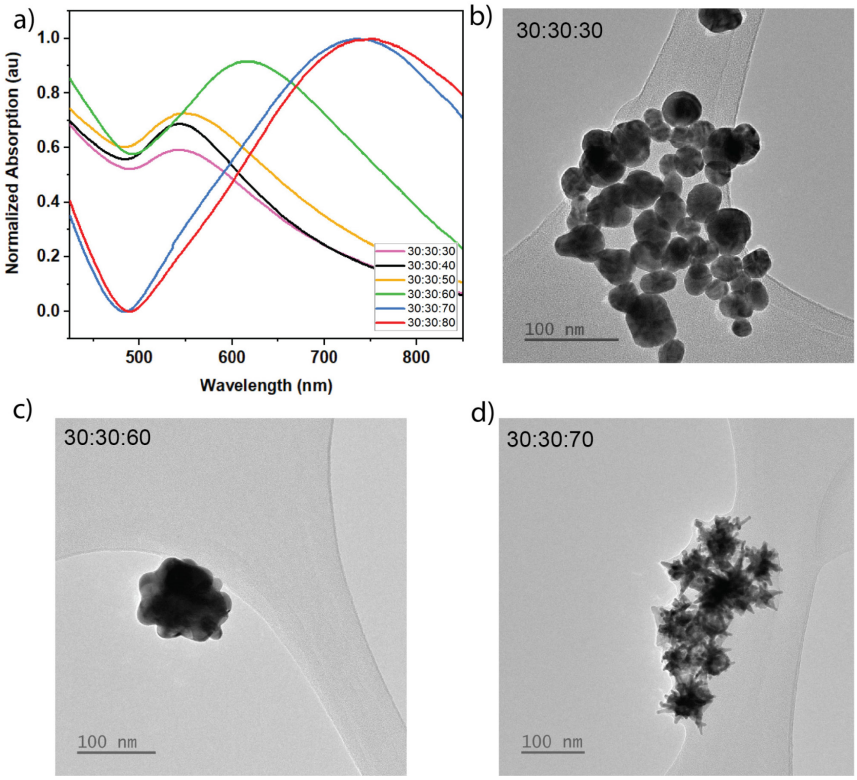

Figure 5. a) UV-Visible spectra of gold nanostars synthesized by vibrating sharp tip microfluidic device by varying ascorbic acid flow rate (30 µL/min to 80 µL/min) with both gold precursor and silver nitrate flow rates constant at 30 µL/min. TEM images of gold nanostars synthesized by vibrating sharp tip device for flow rate ratios of b) 30:30:30 µL/min c) 30:30:60 µL/min d) 30:30:70 µL/min.

First, the influence of ascorbic acid was studied by modifying the flow rate of ascorbic acid and maintaining the constant flow rate of the other two inlets. The total flow rate was kept at a moderate rate 90 µL/min to 150 µL/min. As shown in the Fig. 4, the total flow rate is not expected to influence properties of resulting nanostars in this flow rate range. To study the influence of ascorbic acid concentration, we maintained constant flow rates of the silver and gold at 30 µL/min each while increasing the ascorbic acid flow rate in 10 µL intervals from 30 µL/min to 80 µL/min. As the flow rate of the ascorbic acid is increased in the device, the molar concentration of ascorbic acid passing through the mixer increased from 530 µM to 910 µM. When the concentration of ascorbic acid is increased, the resulting UV-Vis spectra are red-shifted due to the growth phase being favored over nucleation (Silvestri et al. 2017), indicating larger more anisotropic nanostars (**Fig. 5a)**. In this seedless gold nanostar synthesis, the ascorbic acid is the reducing agent that reduces Au^{3+} to Au^{0}, where the rapid reduction of gold initiates nanostar growth. Because ascorbic acid is a weak acid, increasing its concentration influences the reaction pH, thus affecting the reactivity. The significant red shift from the 3:3:6 condition to the 3:3:7 indicates the critical 860 µM concentration of ascorbic acid needed to trigger anisotropic growth into nanostars (Vang and Strobbia 2023). When the infusion rate of ascorbic acid is below 800 µM gold nanospheres are produced rather than gold nanostars (**Fig. 5a and 5b**). Gold nanospheres exhibit optical absorption between 500 nm and 600 nm due to their < 100 nm size and spherical shape.(Haiss et al. 2007; Amendola and Meneghetti 2009) When the ascorbic acid concentration is at 800 µM semi-starlike structures are grown. However, they do not exhibit strong anisotropic branch growth (**Fig. 5c**). At ascorbic acid concentrations at and above the 860 µM condition, highly anisotropic nanostars are produced with diameters ranging from 65 nm to 90 nm (**Fig. 5d**).

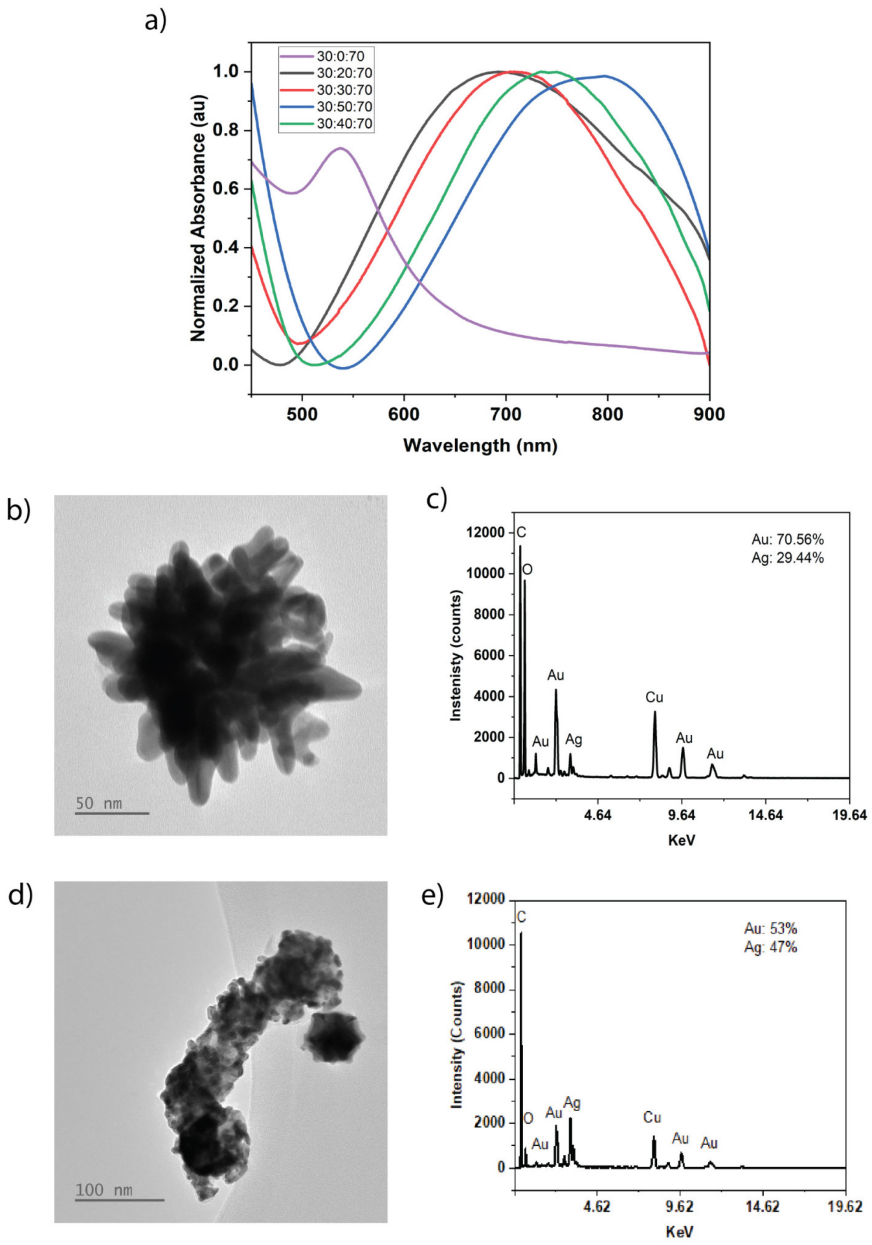

Figure 6. a) UV-Visible spectra of gold nanostars synthesized by vibrating sharp tip microfluidic device by varying silver nitrate flow rate (0 µL/min to 50 µL/min) with gold precursor flow rate constant at 30 µL/min and ascorbic acid flow rate constant at 70 µL/min. b) TEM image of gold nanostars synthesized by vibrating sharp tip microfluidic device with flow rate ratio of 30:30:70 µL/min c) EDX spectra of gold nanostars synthesized with 30:30:70 µL/min flow rate ratio c) TEM images of gold nanostars synthesized by vibrating sharp tip microfluidic device with flow rate ratio of 30:50:70 µL/min e) EDX spectra of gold nanostars synthesized with 30:50:70 µL/min flow rate ratio.

Next, the influence of silver nitrate concentration was studied in a similar manner as for ascorbic acid. The concentration of silver nitrate added to the reaction influences the branching and size in the resulting nanostars. Ag^{+} ions can direct the anisotropic growth

of gold nanoparticle seeds when forming gold nanostars.(Yuan et al. 2012) Preferential adsorption of silver halides onto the crystal facets of the gold seeds influences the number of branches. In fact, silver ions block the [111] crystal plane, so by increasing the Ag^+ concentration, more planes are blocked from branch growth resulting in hyperbranched particles. (De Silva Indrasekara et al. 2018; Pu et al. 2018) As seen in **Fig. 6a,** increasing the flow rate of silver nitrate from 20 µL/min to 50 µL/min results in an optical redshift by changing to concentration from 670 µM to 1.33 mM. Only gold nanoparticles are produced when silver is absent from the synthesis because silver is not available to direct branch growth. When silver is added at 670 µM to 1.33 mM concentrations, gold nanostars with branching are produced (**Fig. 6b)** As the concentration of silver increased, nanostars began to form and the number of branches with also increase due to silver absorption on the gold [111] planes (**Table 1**). When the ratio is increased from 0 µM to 670 µM, nanostars are formed with 11 ± 2 number of branches. When the ratio is further increased from 670 µM to 1.03 mM, the branches increased to 16 ± 4 branches. Interestingly, as the number of branches increases, the length of the branches decreases (**Table 1**). From the HR-TEM image shown in **Fig. 6d**, we can see that when the ratio of gold to silver increases to 1.33 mM, the resulting particles are spherical with no branching. The EDX analysis (**Fig. 6e**) of these particles shows they contain almost ~50% gold and ~50% silver 50%. Unlike the nanostars, which contain ~70% gold and ~30% silver (**Fig. 6c**). We can infer that when the effective molar ratio of gold precursor to silver nitrate reaches 1.33 mM, the resulting nanoparticles will no longer be highly anisotropic with sharp branches. Instead, they are rough, agglomerated nanospheres.

Gold nanostars were also synthesized using a bulk technique to verify the results from our on-chip synthesis. Gold nanostars were synthesized by changing the input volume of the silver nitrate or ascorbic acid in the reaction vessel. By varying the volume of silver nitrate or ascorbic acid, the optical absorption was tuned (**Fig. S3**). These results indicate that we successfully translated the synthesis to the microfluidic device without compromising the reaction. In comparison to bulk synthesis, it is much simpler to control the reaction by using the microfluidic device. Nanostars with varied morphology could be easily synthesized in a single experiment. Unlike with bulk synthesis, separate reactions had to be prepared.

Table 1 summarizes the properties of gold nanostars synthesized using varying concentrations of ascorbic acid and silver. We used TEM imaging and NanoSight nanoparticle tracking analysis (NTA) to determine the average diameter and size distribution of the nanostars. The diameter from TEM imaging was measured from branch tip to tip. TEM measurements were in agreement with the Nanosight (**Table 1**). The resulting size distributions for the samples were used to calculate the polydispersity index (PDI), where PDI is defined as the square of the standard deviation (σ) of the particle diameter distribution divided by the mean particle diameter.

$$\text{PDI} = \left(\frac{\sigma}{d}\right)^2$$

According to dynamic light scattering (DLS) manufacturer specifications, when the PDI is < 0.1, the nanoparticles are considered highly monodisperse. Since nanostars are not

spherical in shape, DLS and particle tracking techniques exhibit more computational error when calculating the hydrodynamic diameter. Nanoparticle tracking analysis, which we used for our measurement, offers improved size distribution results for non-spherical particles (Ribeiro et al. 2018). From our experiments, PDI values for all synthesized particles approached 0.1 and were less than 0.2, which we consider a suitable value for nonspherical particles. Several reports for nanoparticles indicate that PDIs less than 0.2 are well-suited for the nanoparticles (Smith et al. 2003; Danaei et al. 2018).

Ratio Gold:silver:ascorbic acid (µL/min)	**TEM (nm)**	**Nanosight (nm)**	**PDI**	**Branch Length (nm)**	**Number of Branches**
30:0:30	30.5	N/A	0.09 ± 0.1	No branching	No branching
30:30:30	30.5	N/A	0.09 ± 0.1	No branching	No branching
30:30:40	30.5	N/A	0.09 ± 0.1	No branching	No branching
30:30:50	30.5	N/A	0.09 ± 0.1	No branching	No branching
30:30:60	64.1	65.2	0.11 ± 0.1	16.9 ± 5.7	14 ± 1
30:30:70	78.0	77.2	0.12 ± 0.01	17.9 ± 5.4	14 ± 2
30:30:80	93.4	94.6	0.10 ± 0.05	14.7 ± 4.9	14 ± 2
30:0:70	30.6	N/A	0.09 ± 0.1	No branching	No branching
30:20:70	84.4	72.2	0.11 ± 0.01	24.7 ± 8.5	11 ± 2
30:40:70	82.9	75.4	0.12 ± 0.07	14.1 ± 4.5	16 ± 4
30:50:70	79.0	88.5	0.09 ± 0.03	No branching	No branching

Table 1. Nanostar diameter (branch to branch), PDI measurements, and branching analysis from TEM images and nanoparticle tracking analysis. N = 50 particles

All nanostars synthesized with our device were less than 100 nm in diameter, where the diameter from branch to branch is modified by changing the ascorbic acid flow rates. As the flow rate of ascorbic acid increases from 60 µL/min to 80 µL/min the diameter increases from 64.1 nm to 93.4 nm, which is consistent with the red-shift in the UV-Visible spectrum. Additionally, the branching properties are tuned by controlling the silver nitrate flow rate. As the flow rate of silver increases, the number of branches increases with a decrease in branch length, due to the silver ions binding with the [111] planes. Then, when the flow rate reaches 50 µL/min there is no obvious branching. Collectively, the present device offers simple tunability and control of the nanostars synthesis. Users only need to modify the input flow rates to synthesize the nanostars with different sizes and number of branches. From these results, the presented device offers morphological and optical property tuning by modulating the flow rates. Spherical nanoparticles, hyperbranched gold nanostars, and biometallic nanoparticles can be synthesized.

Gold nanostars were also synthesized using a bulk technique to compare the results from our on-chip synthesis. Gold nanostars were synthesized by changing the input volume of the silver nitrate or ascorbic acid in the reaction vessel. First, the gold precursor was added to the reaction vessel, then the silver nitrate was added. Immediately, the ascorbic acid was added and mixed quickly using pipetting. The nanostars were allowed to grow for 20 minutes before washing and resuspension. By varying the volume of silver nitrate or ascorbic acid, the optical absorption was tuned (**Fig. 7**). When controlling the ascorbic acid concentration in the bulk synthesis, gold nanostars are only produced when the ascorbic acid concentration reaches 860 µM by adding 70 µL of ascorbic acid (**Fig. 7a**). Gold nanostars were produced at 800 µM ascorbic acid concentration when using the microfluidic device. In bulk synthesis, optical tunability is limited to synthesizing gold nanospheres and gold nanostars within the 725 to 750 nm region, while for the microfluidic device, the tunability is extended to 650 nm to 750 nm. When the silver concentration was modified, the resulting nanostars yielded close optical absorptions from 750 nm to 800 nm (**Fig. 7b)**. We achieved more controlled optical tunability across 700 to 800 nm by controlling the silver nitrate flow rate by using microfluidic synthesis which enabled tunability from 600 to 800 nm. In comparison to bulk synthesis, it is much simpler to control the reaction by using the microfluidic device. Nanostars with varied morphology could be easily synthesized in a single experiment. Unlike in the bulk synthesis, separate reactions had to be prepared, and the reactions relied on a manual mixing strategy.

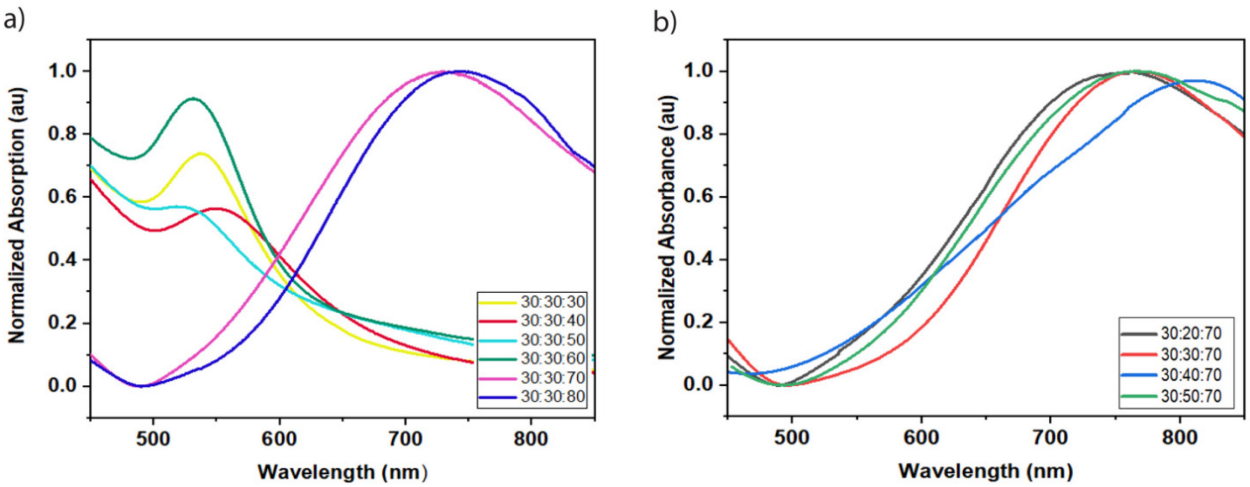

Figure 7. UV-Visible spectra of gold nanostars synthesized by bulk method a) varied ascorbic acid concentration b) varied silver nitrate concentration

Gold nanostar stability and reproducibility

Nanoparticle stability and reproducibility are two critical factors for good synthesis methods. We evaluated the nanostars synthesized via the present method for both metrics. Nanostars synthesized under the same reaction conditions but on a different day with a different user demonstrate comparable LSPR peaks on the UV-Vis spectra (**Fig. 8a**), indicating that the nanostars were reproducible in terms of size and shape. Stability was evaluated by synthesizing nanoparticles under the same reaction conditions and

storing the particles at 4°C for two weeks after washing. As shown in **Fig. 8b**, the particles optical absorption is comparable to the as-synthesized absorption, which shows that proper storage ensures stable nanostars. The slight red shift in the spectra can be attributed to minor aggregation that might have occurred from residual reagents post-washing. Fig. S4 shows the stability of the bulk synthesized gold nanostars and we can see there is a larger red-shift in the optical spectrum indicating greater aggregation of the nanostar samples.

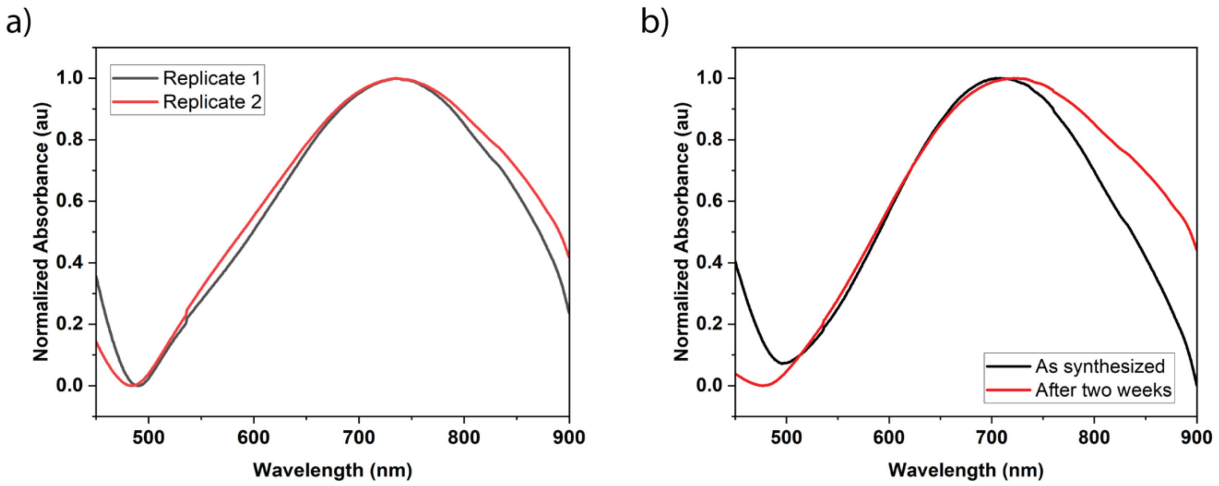

Figure 8. a) Reproducibility and b) stability evaluation of gold nanostar synthesized by vibrating sharp tip microfluidic device

Conclusion

A 3D printed microfluidic device with a vibrating sharp tip mixer was applied for the controlled synthesis of gold nanostars. To date, complex nanostructures, such as gold nanostars have not been synthesized in 3D printed microfluidics. The 3D printed microfluidic enabled the simple integration of the vibrating sharp tip mixer. The highly efficient acoustic mixing enables uniform reagent mixing in as low as 7 ms for rapid nucleation during nanostar synthesis, thus producing high-quality gold nanostars. Compared to bulk synthesis methods, the microfluidic mixing device offers simple, hands-off reagent control for optical property modulation. The vibrating sharp tip mixer has low power requirements (2 – 45 mW). Nanostars with optical absorptions ranging from 650 nm to 800 nm were synthesized by varying the input flow rates for silver nitrate and ascorbic acid. Varying the concentration of ascorbic acid demonstrated shift in the size of nanostars while varying the silver concentration controlled the number of branches. The seedless and surfactant-free synthesis simplifies the synthesis method by eliminating reaction steps and particle post-processing. The device feasibility demonstrated in this work offers an advantageous microfluidic synthesis strategy for other complex metallic nanoparticle structures.

Acknowledgments

This work was supported in part by the National Institute of Health (R01GM135432) and National Science Foundation (ECCS-2144216). KC thanks the support of the NSF

Graduate Research Fellowship Program (GRFP) grant (#13300542). This work acknowledges the use of WVU Shared Research Facilities

References

Abalde-Cela S, Taladriz-Blanco P, de Oliveira MG, Abell C (2018) Droplet microfluidics for the highly controlled synthesis of branched gold nanoparticles. Sci Rep 8:2440. https://doi.org/10.1038/s41598-018-20754-x

Ahmed D, Mao X, Juluri BK, Huang TJ (2009) A fast microfluidic mixer based on acoustically driven sidewall-trapped microbubbles. Microfluidics and Nanofluidics 7:727–731. https://doi.org/10.1007/s10404-009-0444-3

Amendola V, Meneghetti M (2009) Size Evaluation of Gold Nanoparticles by UV−vis Spectroscopy. J Phys Chem C 113:4277–4285. https://doi.org/10.1021/jp8082425

Andrea Cristaldi D, Labanca A, Donal Pottinger T, et al (2021) 3D printed reactor-in-a-centrifuge (RIAC): Making flow-synthesis of nanoparticles pump-free and cost-effective. Chemical Engineering Journal 425:130656. https://doi.org/10.1016/j.cej.2021.130656

Atta S, Beetz M, Fabris L (2019) Understanding the role of AgNO3 concentration and seed morphology in the achievement of tunable shape control in gold nanostars. Nanoscale 11:2946–2958. https://doi.org/10.1039/C8NR07615D

Bachman H, Chen C, Rufo J, et al (2020) An acoustofluidic device for efficient mixing over a wide range of flow rates. Lab on a Chip 20:1238–1248. https://doi.org/10.1039/C9LC01171D

Bandulasena MV, Vladisavljević GT, Odunmbaku OG, Benyahia B (2017) Continuous synthesis of PVP stabilized biocompatible gold nanoparticles with a controlled size using a 3D glass capillary microfluidic device. Chemical Engineering Science 171:233–243. https://doi.org/10.1016/j.ces.2017.05.035

Belliveau NM, Huft J, Lin PJ, et al (2012) Microfluidic Synthesis of Highly Potent Limit-size Lipid Nanoparticles for In Vivo Delivery of siRNA. Molecular Therapy - Nucleic Acids 1:e37. https://doi.org/10.1038/mtna.2012.28

Boleininger J, Kurz A, Reuss V, Sönnichsen C (2006) Microfluidic continuous flow synthesis of rod-shaped gold and silver nanocrystals. Phys Chem Chem Phys 8:3824–3827. https://doi.org/10.1039/B604666E

Bressan LP, Lima TM, Da Silveira GD, Da Silva JAF (2020) Low-cost and simple FDM-based 3D-printed microfluidic device for the synthesis of metallic core–shell nanoparticles. SN Appl Sci 2:984. https://doi.org/10.1007/s42452-020-2768-2

Bressan LP, Robles-Najar J, Adamo CB, et al (2019) 3D-printed microfluidic device for the synthesis of silver and gold nanoparticles. Microchemical Journal 146:1083–1089. https://doi.org/10.1016/j.microc.2019.02.043

Chatterjee S, Ringane AB, Arya A, et al (2016) A high-yield, one-step synthesis of surfactant-free gold nanostars and numerical study for single-molecule SERS application. J Nanopart Res 18:242. https://doi.org/10.1007/s11051-016-3557-0

Chen H, Di Y, Chen D, et al (2015) Combined chemo- and photo-thermal therapy delivered by multifunctional theranostic gold nanorod-loaded microcapsules. Nanoscale 7:8884–8897. https://doi.org/10.1039/C5NR00473J

Chen Z, Liu P, Zhao X, et al (2021) Sharp-edge acoustic microfluidics: Principles, structures, and applications. Applied Materials Today 25:101239. https://doi.org/10.1016/j.apmt.2021.101239

Danaei M, Dehghankhold M, Ataei S, et al (2018) Impact of Particle Size and Polydispersity Index on the Clinical Applications of Lipidic Nanocarrier Systems. Pharmaceutics 10:57. https://doi.org/10.3390/pharmaceutics10020057

De Silva Indrasekara AS, Johnson SF, Odion RA, Vo-Dinh T (2018) Manipulation of the Geometry and Modulation of the Optical Response of Surfactant-Free Gold Nanostars: A Systematic Bottom-Up Synthesis. ACS Omega 3:2202–2210. https://doi.org/10.1021/acsomega.7b01700

D. Ramsey J, Zhou L, Almlie CK, et al (2015) Achieving plasmon reproducibility from surfactant free gold nanostar synthesis. New Journal of Chemistry 39:9098–9108. https://doi.org/10.1039/C5NJ01590A

Enders A, Siller IG, Urmann K, et al (2019) 3D Printed Microfluidic Mixers—A Comparative Study on Mixing Unit Performances. Small 15:1804326. https://doi.org/10.1002/smll.201804326

Haiss W, Thanh NTK, Aveyard J, Fernig DG (2007) Determination of Size and Concentration of Gold Nanoparticles from UV−Vis Spectra. Anal Chem 79:4215–4221. https://doi.org/10.1021/ac0702084

He Z, Wang J, Fike BJ, et al (2021) A portable droplet generation system for ultra-wide dynamic range digital PCR based on a vibrating sharp-tip capillary. Biosensors and Bioelectronics 191:113458. https://doi.org/10.1016/j.bios.2021.113458

Herbst M, Hofmann E, Förster S (2019) Nucleation and Growth Kinetics of ZnO Nanoparticles Studied by in Situ Microfluidic SAXS/WAXS/UV–Vis Experiments. Langmuir 35:11702–11709. https://doi.org/10.1021/acs.langmuir.9b01149

Huang P, Zhao S, Bachman H, et al (2019) Acoustofluidic Synthesis of Particulate Nanomaterials. Adv Sci 6:1900913. https://doi.org/10.1002/advs.201900913

Illath K, Shinde A, Paremmal P, et al (2023) Surface plasmon resonance tunable gold nanostar synthesis in a symmetric flow-focusing droplet device. Surfaces and Interfaces 36:102478. https://doi.org/10.1016/j.surfin.2022.102478

Jahn A, Stavis SM, Hong JS, et al (2010) Microfluidic Mixing and the Formation of Nanoscale Lipid Vesicles. ACS Nano 4:2077–2087. https://doi.org/10.1021/nn901676x

Khoury CG, Vo-Dinh T (2008) Gold Nanostars For Surface-Enhanced Raman Scattering: Synthesis, Characterization and Optimization. J Phys Chem C 112:18849–18859. https://doi.org/10.1021/jp8054747

Kimura N, Maeki M, Sato Y, et al (2018) Development of the iLiNP Device: Fine Tuning the Lipid Nanoparticle Size within 10 nm for Drug Delivery. ACS Omega 3:5044–5051. https://doi.org/10.1021/acsomega.8b00341

Kitson PJ, Rosnes MH, Sans V, et al (2012) Configurable 3D-Printed millifluidic and microfluidic 'lab on a chip' reactionware devices. Lab Chip 12:3267. https://doi.org/10.1039/c2lc40761b

Kumar PS, Pastoriza-Santos I, Rodríguez-González B, et al (2007) High-yield synthesis and optical response of gold nanostars. Nanotechnology 19:015606. https://doi.org/10.1088/0957-4484/19/01/015606

Li X, He Z, Li C, Li P (2021) One-step enzyme kinetics measurement in 3D printed microfluidics devices based on a high-performance single vibrating sharp-tip mixer. Analytica Chimica Acta 1172:338677. https://doi.org/10.1016/j.aca.2021.338677

Li Y, Huang X, Lee R, et al (2016) Synthesis of Polymer-Lipid Nanoparticles by Microfluidic Focusing for siRNA Delivery. Molecules 21:1314. https://doi.org/10.3390/molecules21101314

Liebig F, Henning R, Sarhan RM, et al (2019) A simple one-step procedure to synthesise gold nanostars in concentrated aqueous surfactant solutions. RSC Adv 9:23633–23641. https://doi.org/10.1039/C9RA02384D

Ma J, Lee SM-Y, Yi C, Li C-W (2017) Controllable synthesis of functional nanoparticles by microfluidic platforms for biomedical applications – a review. Lab Chip 17:209–226. https://doi.org/10.1039/C6LC01049K

Maeki M, Saito T, Sato Y, et al (2015) A strategy for synthesis of lipid nanoparticles using microfluidic devices with a mixer structure. RSC Adv 5:46181–46185. https://doi.org/10.1039/C5RA04690D

Marelli M, Bossola F, Spinetti G, et al (2020) Microfluidic Synthesis of Hybrid TiO_2 - Anisotropic Gold Nanoparticles with Visible and Near-Infrared Activity. ACS Appl Mater Interfaces 12:38522–38529. https://doi.org/10.1021/acsami.0c08241

Minati L, Benetti F, Chiappini A, Speranza G (2014) One-step synthesis of star-shaped gold nanoparticles. Colloids and Surfaces A: Physicochemical and Engineering Aspects 441:623–628. https://doi.org/10.1016/j.colsurfa.2013.10.025

Nama N, Huang P-H, Huang TJ, Costanzo F (2016) Investigation of micromixing by acoustically oscillated sharp-edges. Biomicrofluidics 10:024124. https://doi.org/10.1063/1.4946875

Nehl CL, Liao H, Hafner JH (2006) Optical Properties of Star-Shaped Gold Nanoparticles. Nano Lett 6:683–688. https://doi.org/10.1021/nl052409y

Pandey S, Thakur M, Mewada A, et al (2013) Carbon dots functionalized gold nanorod mediated delivery of doxorubicin: tri-functional nano-worms for drug delivery, photothermal therapy and bioimaging. J Mater Chem B 1:4972. https://doi.org/10.1039/c3tb20761g

Phiri MM, Mulder DW, Vorster BC (2019) Seedless gold nanostars with seed-like advantages for biosensing applications. R Soc open sci 6:181971. https://doi.org/10.1098/rsos.181971

Pu Y, Zhao Y, Zheng P, Li M (2018) Elucidating the Growth Mechanism of Plasmonic Gold Nanostars with Tunable Optical and Photothermal Properties. Inorg Chem 57:8599–8607. https://doi.org/10.1021/acs.inorgchem.8b01354

Ranganathan N, Li C, Suder T, Karanji A K, Li X, He Z, Valentine S, Li P (2019) Capillary Vibrating Sharp-Edge Spray Ionizatoin (cVSSI) for Voltage-Free Liquid Chromatography- Mass Spectrometry. *J. Am. Soc. Mass Spectrom.* 2019, 30, 5, 824–831 https://doi.org 10.1007/s13361-019-02147-0

Ribeiro LN de M, Couto VM, Fraceto LF, de Paula E (2018) Use of nanoparticle concentration as a tool to understand the structural properties of colloids. Sci Rep 8:982. https://doi.org/10.1038/s41598-017-18573-7

Sebastian Cabeza V, Kuhn S, Kulkarni AA, Jensen KF (2012) Size-Controlled Flow Synthesis of Gold Nanoparticles Using a Segmented Flow Microfluidic Platform. Langmuir 28:7007–7013. https://doi.org/10.1021/la205131e

Silvestri A, Lay L, Psaro R, et al (2017) Fluidic Manufacture of Star-Shaped Gold Nanoparticles. Chem Eur J 23:9732–9735. https://doi.org/10.1002/chem.201701617

Smith J, Menger M, Carrion M, Butman BT (2003) 519. A Dynamic Light Scattering (DLS) Assay for the Analysis of Aggregated Adenovector Particles. Molecular Therapy 7:S202–S203. https://doi.org/10.1016/S1525-0016(16)40961-5

Tofighi G, Lichtenberg H, Pesek J, et al (2017) Continuous microfluidic synthesis of colloidal ultrasmall gold nanoparticles: in situ study of the early reaction stages and application for catalysis. Reaction Chemistry & Engineering 2:876–884. https://doi.org/10.1039/C7RE00114B

Uson L, Sebastian V, Arruebo M, Santamaria J (2016) Continuous microfluidic synthesis and functionalization of gold nanorods. Chemical Engineering Journal 285:286–292. https://doi.org/10.1016/j.cej.2015.09.103

Valencia PM, Basto PA, Zhang L, et al (2010) Single-Step Assembly of Homogenous Lipid−Polymeric and Lipid−Quantum Dot Nanoparticles Enabled by Microfluidic Rapid Mixing. ACS Nano 4:1671–1679. https://doi.org/10.1021/nn901433u

Vang D, Strobbia P (2023) Analysis of Nanostar Reshaping Kinetics for Optimal Substrate Fabrication. Appl Spectrosc 77:270–280. https://doi.org/10.1177/00037028221132525

Yuan H, Khoury CG, Hwang H, et al (2012) Gold nanostars: surfactant-free synthesis, 3D modelling, and two-photon photoluminescence imaging. Nanotechnology 23:075102. https://doi.org/10.1088/0957-4484/23/7/075102